Bedding Effect of Carbonaceous Slate Failure Behavior at Direct Shear Tests

Han Wang
Liaoning Institute of Science and Technology
Fuqiang Ren (renfuqiangcumtb@163.com)
University of Science and Technology Liaoning
Yuan Chang
University of Science and Technology LiaoNing

Research Article

Keywords: Carbonaceous slate, direct shear test, bedding effect, dissipated energy, frequency band

Posted Date: March 18th, 2021

DOI: https://doi.org/10.21203/rs.3.rs-309632/v1

Bedding Effect of Carbonaceous Slate Failure Behavior at Direct Shear Tests

Han Wang, Fuqiang Ren*, Yuan Chang

School of Civil Engineering, University of Science and Technology LiaoNing, Anshan 114051, China

Corresponding author: Fuqiang Ren

Email address: renfuqiangcumtb@163.com

Abstract: In this study, the carbonaceous slate of Muzhailing tunnel was selected to explore the deformation and failure mechanism of tunnel layered slate under direct shear conditions. Five sets of direct shear tests were carried out on slate with different bedding dip angles (β: 0°, 30°, 45°, 60°, and 90°). The strength parameters, failure mode, fracture topography, dissipated energy, and acoustic emission (AE) characteristics were analyzed in detail to study the bedding effect of slate failure. The results show that the cohesion and internal friction angle of slate increases and decreases linearly with β from 0° to 90°, respectively, and the shear strength of bedding plane is lower than that of matrix. Additionally, the relative roughness (δ) of gray-scale image was defined, and the linear relationship between δ and root-mean-square height (S_q) was established to improve the efficiency of evolution of fracture topography. Furthermore, the shear energy consumption per unit area (u_s) was calculated, less sensitive to the variation of β. Moreover, a larger AE count and energy release rate were observed when the shear stress decreased, and a relative quiet period was observed before the peak loading. Additionally, both the count and energy release rate linearly decreased with the increase in β, and the proportion of tensile microcracks for vertical bedding is slightly higher than that for horizontal bedding. The main frequency of vertical bedding slate is smaller than that of horizontal bedding, i.e., the size of microcracks of slate with β of 90° is relatively larger. Generally, the frequency bandwidth of slate became narrower when β was varied from 30° to 60°, and the main frequency increased, indicating that the degree of shear failure of matrix is weakened. In contrast, the degree of cracking along the bedding plane increased.

Keywords: Carbonaceous slate, direct shear test, bedding effect, dissipated energy, frequency band

Nomenclature

β	Bedding dip angle of slate: the angle between the bedding plane and the horizontal plane
u_s	Shear energy consumption per unit area

U_e, U_r, U_d	Elastic, residual, and dissipated strain energy, respectively
W, W_n, W_s	The work done by the external, normal and tangential loads
U_1, U_2	Positive and negative work done by the normal load
A_e	Effective shear area
S_q	Root-mean-square height
A	Scanning area
x, y, z	Coordinates of the fracture topography
δ	Relative roughness
$SD_{gray\ matrix}$	Standard deviation of gray matrix
$M_{gray\ matrix}$	Mean value of gray matrix
τ_p, τ_r	Peak and residual shear stresses
τ, σ_n	Shear and normal stresses
c, φ	Cohesion and internal friction angle
RA	Rise time divide by amplitude

1. Introduction

Bedding-plane orientation is one of the important factors affecting the mechanical behavior of engineering rock masses (Ning et al, 2011; He et al., 2012; Liu et al., 2018). The study of effect of bedding dip angle (β) on the mechanical behavior of different lithological rock masses has guiding significance for engineering issues such as shale gas (Sun et al., 2016; Xie et al., 2020; Suo et al., 2020) and metal and coal mining (Pomeroy et al., 1971; Maruvanchery 2020, Zhu et al., 2020), and underground tunnel excavation (Lisjak et al., 2015). For example, during hydraulic fracturing, the bedding-plane cracking of shale often precedes the cracking of matrix, thereby inhibiting the formation of fracture networks and reducing the efficiency of hydraulic fracturing (Stanek and Eisner, 2017; James et al., 2016). Additionally, when a tunnel passes through the strata containing horizontal or inclined rock stratum, the tunnel surrounding rock tends to fail first at the arch shoulder or vault (Tao

et al., 2020). Therefore, it is essential to better understand the strength, failure mode, and failure mechanism of surrounding rock under the influence of β for the safety and efficient exploration of underground resources or space.

Anisotropy characteristic is a typical property of layered rock mass; many studies have been conducted on rock anisotropy (Taliercio and Landriani, 1988; Ramamurthy, 1993). Jaeger et al. (1960) studied the anisotropy of elastic parameters of layered rock in detail using theoretical and experimental methods. A triaxial compression test of rock-like materials was carried out (Tian and Kuo, 2001). The relationship between their mechanical parameters and bedding orientation was analyzed, and the failure criterion for transversely isotropic rock was established. Behrestaghi et al. (1996) studied the anisotropic characteristics of Schist's elastic modulus, Poisson's ratio, and other mechanical parameters under unidirectional compressive stress and established a transversely isotropic constitutive model of Schist. Additionally, Claession et al. (2002) established theoretical formulas for the elastic constant and tensile strength of anisotropic rock considering the bedding orientation. Aliabadian et al. (2019) studied the tensile strength, crack length, and energy dissipation characteristics of layered sandstone under indirect tensile load. Heng et al. (2014) conducted an experimental study on the strength anisotropy characteristics of shale under direct shear conditions. Ikari et al. (2015) studied the effect of difference angle between shale bedding plane and shear force on macroscopic fracture evolution under biaxial shear tests. Hence, previous studies about the anisotropic characteristics of rock involve multiple load forms (uniaxial and triaxial compression, indirect and direct tension, direct shear, etc.) and lithologies (sandstone, slate, shale, schist, rock-like materials, etc.)

The internal mechanism of shear fracture of rock under shear stress is complex. Therefore, a better understanding of the mechanism of bedding orientation on the propagation and evolution of shear fractures has an important guiding role in explaining macroscopic fracture (Virgo et al., 2013). Amann et al. (2011) reported that under low confining pressure conditions, the axial splitting failure is dominated when the angle between bedding plane and loading direction is vertical. Additionally, as the confining pressure increases, the fracture angle gradually decreases, and the fracture mechanism gradually becomes shearing. The shear failure of bedding plane and through-bedding is the main factor, i.e., the effect of bedding orientation on fracture mechanism is reduced under a high confining pressure. Compared with the triaxial compression test method, a direct shear test can overcome the uncertainty of shear fracture surface and randomness of crack

initiation in the study of shear crack evolution mechanism. Carey et al. (2015) used X-ray tomography to analyze the crack propagation of shale during direct shear, explaining the formation mechanism of shear fracture zone. Tatone and Grasselli (2014) also used X-ray micro-CT technology to study the effect of magnitude of normal stress on the topography of discontinuous surface during direct shear. Cheng et al. (2019) explored the whole process of initiation, propagation, and penetration of mesoscopic cracks in the shearing of coal and reported that tension and shear fracture coexist during shearing. However, the mechanical behavior of layered rock formations of different lithologies is also quite different. At present, the quantitative relationship between the shear strength parameters of slate and β should be further studied, and few studies focused on the bedding effect of failure behavior and involve the energy dissipation characteristics. Therefore, this study aims to systematically evaluate the bedding effect of shear failure of carbonaceous slate through direct shear tests and discuss the energy dissipation characteristics during shearing and the formation mechanism of macroscopic shear fracture. Specifically, five sets of direct shear tests were carried out on slates with different β, and an acoustic emission (AE) system was used to monitor the microcracks evolution in shear failure. Furthermore, the shear strength parameters, failure modes, energy consumption, AE activities, energy release, and time-frequency characteristics of typical waveforms were systematically analyzed to evaluate the effect of β on the mechanical behavior of slate failure.

2. Materials and methods

2.1 Materials

Slate samples were collected from Muzhailing tunnel, Gansu province in Northwest China. The length of tunnel (direction is N71°E) is 1813 m, and the maximum buried depth is 591 m. Additionally, the *in-situ* stress direction is N34°E, and the maximum horizontal principal stress is 24.95 MPa. Moreover, the major surrounding rock is a moderately weathered slate (grade V surrounding rock). Fig. 1a shows the engineering geology profile of Muzhailing tunnel. The sampling area is located at tunneling face (excavation footage 530 m). From the view of AA′ section (Fig. 1b), the dip angle of slate is ~45°, and the typical rock element in different positions of tunnel has different dip angles. For example, at the left shoulder of tunnel, the bedding plane of rock element is vertical (β is 90°). Actually, in field, the left shoulder of tunnel has severe deformation (Fig. 1c); the bending and shear failure were obvious under the support of steel arch.

The slate was processed into cylinders with diameters and heights of 50 mm and 50 mm, respectively, as shown in Fig. 2a. The 25 samples were divided into five groups according to the bedding dip angle (β = 0°, 30°, 45°, 60°, and 90°), the angle between bedding plane and horizontal plane. Additionally, four samples of each group were tested with different normal stresses (5 MPa, 10 MPa, 15 MPa, 20 MPa), and the remaining one was used as a spare sample. Before the tests, X-ray diffraction (XRD) analysis of slate samples was performed. The major minerals present in the slate are quartz (43.8%), potassium feldspar (1.0%), plagioclase (2.2%), and clay minerals (53.0%, illite dominant). Additionally, as shown in Fig. 2b, the scanning electron microscopy image shows the obvious lamellar structure inside the slate.

2.2 Experimental method

Direct shear tests were conducted using a true triaxial electrohydraulic servo-controlled loading system (Fig. 3a). Fig. 3a also shows the photograph of direct shear device. Fig. 3b shows the corresponding schematic of direct shear test. Antifriction rollers were set between pressure plate and pressure head to reduce the friction; additionally, a Teflon antifriction shim was set between the upper and lower shear box to reduce friction. The normal stress was first loaded on specimen with a loading rate of 0.5 kN/s, keeping 100 s to make the stress distributed uniformly. Additionally, the shear stress was loaded at a speed of 0.004 mm/s until specimen failure.

During the test, a Micro-II system produced by the American Physical Acoustics Corporation (PAC) was used for AE monitoring. This system uses an 18-bit A/D switching technology that allows instantaneous time-waveform recording. In this study, the AE signals were amplified to 100 times (the amplifier was set as 40 dB). The threshold, sampling frequency, and sampling length were set as 40 dB, 2 MHz, and 4096 datapoints, respectively. Two Nano-30 sensors with a response frequency of 100-400 kHz were used to acquire the AE signals. The AE sensors were fixed on the surface of upper and lower parts of shear box using glue (Fig. 3b).

2.3 Dissipation energy calculation

It is important to quantitatively evaluate the bedding effect of carbonaceous slate from the perspective of energy dissipation to

better understand the effect of bedding structure on shear mechanical properties. However, considering the anisotropy of slate, it is necessary to standardize the dissipation energy. Additionally, in this study, the shear energy consumption per unit area (u_s, Eq. 1) was taken as the evaluation index.

$$u_s = \frac{U_d}{A_e} \tag{1}$$

$$W = U_e + U_d + U_r \tag{2}$$

$$W = W_n + W_s = W_n + U_1 - U_2 \tag{3}$$

$$U_d = W_n + U_1 - U_2 - U_e - U_r \tag{4}$$

where u_s is the dissipation energy per unit area in direct shear test, U_d is the total dissipation energy, and A_e is the effective shear area. According to the law of conservation of energy, as expressed in Eq. 2, the work done (W) by the external loads on the specimen during the direct shear test was transformed into elastic strain energy (U_e), dissipated strain energy (U_d), and residual strain energy (U_r). Additionally, the work done by external force mainly includes two parts: normal (W_n) and tangential (W_s) work loads, as shown in Eq. 3. Fig. 4 shows a typical load-displacement curve of direct shear test. The peak and residual shear stresses are τ_p and τ_r, respectively. The work done by tangential shear load is the area enclosed by tangential load displacement curve; U_e and U_d are the area of triangles corresponding to the peak and residual stress point, respectively. Moreover, the slope of oblique side of right triangle is the slope of straight line section of tangent load displacement curve. However, the work done by normal load consists of the positive work (U_1) done during the application of normal load to the design value and the negative work (U_2) done when the normal load remains unchanged. Hence, the total dissipation energy can be calculated using Eq. 4.

The effective shear area can be estimated using the binarization digital image of shear fracture after failure, i.e., the effective shear area (Babanouri and Nasab, 2015) is occupied by the white area. Notably, the binarization image is significantly affected by the shooting environment and thresholds. Therefore, the external environment during shooting should be as consistent as possible. Additionally, each shear test consists of two fractures, and the effective shear area is the average of two

sides.

2.4 Fracture topography

The topography of shear fracture can be used to evaluate the shear failure mechanism. As shown in Figs. 5a-c, the three-dimensional (3D) noncontact surface profiler can be used to measure the 3D topography of shear fracture. When the specimen was fixed on the working platform, the position of optical measuring probe was adjusted to maintain the probe and cross-section at 30 mm. Additionally, the scanning area (A) was set as 50*50 mm^2, and the scanning accuracy was set as 20 μm. Each point in the image has the corresponding x, y, and z coordinate values, and the root-mean-square height (S_q, Eq. 5, quantitative description of dispersion degree of fracture surface height distribution) was selected to quantify the fracture topography characteristics (Ju et al., 2019; Zhao et al., 2017).

$$S_q = \sqrt{\frac{1}{A}\iint_A z^2(x,y)dxdy} \tag{5}$$

However, the scanning process of each fracture needs a long time. To improve the experimental efficiency without losing accuracy, the idea of using relative roughness (δ) instead of S_q was proposed based on the gray histogram of digital fracture image. Additionally, δ can be defined as follows:

$$\delta = \frac{\mathrm{SD}_{gray\ matrix}}{\mathrm{M}_{gray\ matrix}} \tag{6}$$

where $\mathrm{SD}_{gray\ matrix}$ and $\mathrm{M}_{gray\ matrix}$ are the standard deviation and mean value of gray matrix, respectively. By testing, S_q has a linear relationship with δ, and the fitting curve (S_q = 2985.14 × δ-1334.64) is shown in Fig. 5d. Therefore, the analysis of subsequent test results can first use the easily obtained δ to convert the S_q of shear fracture and then analyze the shear failure mechanism of slate with different bedding dip angles.

3. Results and discussion

3.1 Strength parameters and failure pattern

The shear stress-displacement curve of slate under different bedding dip angles and normal stresses is shown in Fig. 6. Generally, the overall change trend of shear stress-shear displacement curves of all samples before reaching the peak stress is the same. At the beginning of loading, the slope of curve is small, the shear displacement increases faster, and the shear stress

increases slowly. Because a certain gap exists between the shear box and sample and the initial shear stress has decreased these gaps, when the shear displacement reaches a certain value, the slope of curve increases significantly, and the increase in shear displacement becomes slow. The shear stress increases rapidly, and the shear stress-displacement curve shows a clear yield point. After reaching the peak strength, the slope of curve changes from positive to negative, and the shear stress drop phenomenon may have appeared multiple times. When the shear stress decreases to a certain level, the slope of curve suddenly becomes smooth. As shear displacement continues to increase, the shear stress gradually enters the residual strength stage. At this stage, the shear stress shows the common feature of rock shear failure and sliding (stick-slip, Cloos 1992).

Additionally, the peak shear stress (τ_p) of slate with different β values increases with the increase in normal load, but the tangential displacement of sample at the peak stress is different. Specifically, when β is 0° and 90°, the tangential displacements corresponding to the peak loads are relatively small, about 0.7-1.0 mm and 0.8-1.8 mm, respectively, while β of 30° corresponds to the largest tangential displacement (1.3-3.2 mm). If the β is 45° and 60°, the tangential displacement spans (1.3-2.9 mm and 1.2-2.8 mm, respectively) are similar. Additionally, when the β is 0° and 90°, brittle shear failure occurs only when the normal load is 5 MPa. With the increase in normal load, the stick-slip phenomenon appears, especially when the normal load is 20 MPa. The stress after the peak stress clearly fluctuates with the increase in displacement. When β is 30°, almost no stick-slip phenomenon is observed; when β is 45°, the brittle shear failure characteristics are obvious when the normal stress is less than 20 MPa. When β is 60°, the shear sliding is the most obvious when the normal stress is 15 MPa, and the maximum normal stress corresponds to the minimal shear displacement.

Table 1 shows the peak shear stresses corresponding to different normal stresses of different β slate samples. Additionally, all samples have residual stress after shear failure, and the mean and standard deviation of ratio (τ_r/τ_p) of residual stress to peak stress is also shown in Table 1. The relationship between the ratio (τ_r/τ_p) and β is shown in Fig. 7. As β increases, the ratio first decreases and then increases. When β is 90°, the corresponding value is the largest (0.76), and when β is 45°, the corresponding value is the smallest (0.53). In other words, the stress drop corresponding to vertical bedding is the largest, i.e.,

the brittle failure characteristic is the most obvious, followed by horizontal bedding, and the stress drops corresponding to oblique bedding are smaller (0.53-0.60). According to the Mohr-Coulomb shear strength criterion (Eq. 7, Shen et al., 2018), the corresponding shear strength parameters of slate with different β values were calculated (as shown in Table 1), and the change of cohesion (c) and internal friction angle (φ) of slate with β is shown in Fig. 8.

$$\tau = \sigma_{\mathrm{n}} \tan\varphi + c \tag{7}$$

where c and φ are the cohesion and internal friction angle; τ and σ_{n} are the shear and normal stress. In general, the cohesion and internal friction angle are approximately linear with increasing β. Specifically, the cohesion increases linearly with the increase in β, while the change process of internal friction angle is just the opposite, decreasing linearly with the increase in β. However, the shear strengths of slate with different β from high to low are 45° > 30° > 90°> 60° > 0°, and the shear strengths of slate (30°, 90°, and 60°) are closed.

Fig. 9a shows the failure pattern of shear failure of slate under different normal stresses. For the slate with β of 0°, the integral shear failure along the bedding plane is dominated. When the normal stress is 5 MPa, local protrusions appeared on the shear section. As the normal stress increased, the scratches due to friction on the section became more obvious. When β is 90°, a fracture is formed by the shear failure of matrix and bedding plane. Additionally, the local cracking of vertical bedding plane is also presented, and with the increase in normal stress, the scratches of fracture surface are more obvious. Especially when the normal stress is 20 MPa, fragments are presented in the local area of shear fracture. For slate with β of 30-60°, varying degrees of composite failure of bedding plane cracking and matrix shear failure were observed. For example, when β is 30° and the normal stress is 15 MPa, the stepped tensile fracture is obvious; when β is 45° and the normal stress is 10 MPa, a concave fracture is formed along the bedding plane. When β is 60° and the normal stress is 15 MPa, the cracks along the bedding plane are particularly obvious, and the scratches and fragmented characteristics of fracture are also more obvious.

According to the digital images of typical shear fractures with different β values, a gray histogram was obtained, as shown in Fig. 9b. The fracture topography characteristics of different β values are quite different. According to the calculation method

of δ described in Section 2.4 and the corresponding relationship between δ and the S_q of fracture topography, the S_q of direct shear failure fracture of slate with different β values can be obtained, as shown in Fig. 9c. With the increase in β, the mean value first increases and then decreases and then increases again. When β is 60° and 30°, the minimum and maximum values were obtained. In other words, when β is 60°, the fracture is flatter; when β is 30°, the height fluctuation degree of fracture is the largest. When β is 90°, the elevation dispersion degree of fracture is slightly larger than that of horizontal bedding (0°), and when β is 45°, the shear fracture is relatively flatter compared to vertical and horizontal bedding. Because the protrusions and depressions of shear fracture at 45° only appear as local areas, the protrusions and depressions of slate with vertical and horizontal beddings appear at intervals.

For intact or fractured rock, when shear fracture or shear cracks propagate, the shear strength in a certain area near the crack tip will be weakened by sliding as the shear crack extends (He 1995). For different directions of anisotropic rock masses, the specific signs of slip weakening (SW) are different. When β is 0°, the weakening of shear along the bedding plane becomes more obvious when the normal stress is greater than 5 MPa. When β is 90°, the overall SW phenomenon is weak. Additionally, the shear SW is related to the number and spacing of bedding planes. It is difficult to reflect the SW when the bedding plane spacing is small and the number is large. However, the shear strength of matrix is greater than that of bedding plane. For the slate samples with β of 45°, the bedding plane width (the gray band shown in Fig. 2a) in the shear core area is larger, and the brittleness is more obvious at failures. No obvious SW phenomenon was observed, one of the reasons for the higher shear strength. For the slate with β of 30° and 60°, under the action of shearing, the tensile cracks along the bedding plane caused the local failure of sample. Subsequently during shearing and sliding, the tensile cracks penetrated along the bedding plane, and the connection of shear cracks and tension cracks formed the overall rupture zone. Moreover, the cracks along the bedding plane increased the roughness of shear rupture plane, probably one of the reasons that the shear strengths of slate with β of 30° and 60° are close to vertical bedding.

3.2 Energy consumption

According to the calculation principle of shear dissipated energy as described in Section 2.3, the stress-displacement curves

of 20 slate direct shear tests are processed, and the corresponding dissipated energy of different samples are obtained, as shown in Table 2. However, for a small number of samples, the dissipated energy with a lower normal stress is larger than that with a higher normal stress. This is mainly because the dissipated energy is affected by the number and spacing of bedding planes, which is not the focus of this study. For the direct shear test, the failure of sample is mainly sheared, and most of its dissipated energy is used to generate shear microcracks, causing crack propagation and forming the final shear fracture. Eq. 1 shows that the dissipated energy per unit area can be calculated from the effective shear area. For the shear fracture, the scratch area generated by sliding friction can be approximately equivalent to the effective shear area, and it can provide quantitative estimation of binary image of shear fracture.

The digital images of some typical shear fractures and the corresponding binary images are shown in Fig. 10a. According to the relationship between image pixels and physical size, the area corresponding to the effective shear area (i.e., white area) can be calculated, and the specific values are also shown in Table 2. In general, the corresponding effective shear areas of horizontal (0°) and vertical (90°) bedding plane slate are larger than that of slate with oblique bedding plane; as the normal stress increases, the effective shear area also increases. Table 2 also shows the average value of u_s, and the change of u_s with β is shown in Fig. 10b. As β increases, the u_s first increases, then decreases, and finally increases. However, the variation range of u_s is small (16.17-17.62 mJ/mm^2), indicating that u_s is not sensitive to the variation in β. According to the theory of fracture mechanics, the fracture toughness of a material represents its ability to resist brittle fracture and is an inherent property of the material itself. Therefore, for the direct shear failure of slate with different β values, the shear energy consumption per unit area is less affected by β. Additionally, the main reason for the slight fluctuation is probably the difference in the ability of matrix and bedding plane to resist cracks.

3.3 AE characteristics

AE activity, energy release, and time-frequency characteristics of waveform (Ohtsu, 2008; Ren et al., 2020) can be used to evaluate the development characteristics of microcracks during the slate direct shear test. AE count is one of the commonly

used indicators to characterize AE activity. When β is 0° and the normal stress is 20 MPa, Fig. 11a shows the curve of AE count rate and cumulative AE counts changing with shear stress-time. Fig. 11a shows that the entire loading process can be divided into four stages. In the initial loading stage (Stage I), relatively strong intermittent AE signals are generated, and the cumulative AE count increases slowly. The AE signals from stage I are mainly caused by the internal pores of slate, and the gap between shear box and specimen is closed. The AE signals in the continuous stable deformation stage (Stage II) are obviously much denser, but the overall count rate is relatively small. Additionally, the cumulative count curve is approximately parallel to the loading curve. This indicates that the rate of occurrence of microcracks is relatively stable, and the growth rate is the fastest during the entire loading. At the end of stage II, the shear stress has a small stress drop, corresponding to a larger count rate. In the unstable deformation stage (Stage III), the number of AE signals is small, and the cumulative count increases slowly at a lower rate. Hence, stage III experienced the effect of previous stage of stress release and entered a relatively quiet period. In addition, the energy is gradually accumulated and released suddenly during the peak stress, producing more AE signals, and the cumulative counts increase suddenly. Stage IV is the post-peak deformation stage. In this stage, the AE signal is intermittently enhanced until the end of the test, and the cumulative AE count increases approximately in steps.

Fig. 11b shows the change in AE energy release rate and cumulative released energy with the shear stress-time curve when β is 0° and the normal stress is 20 MPa. The curve can also be divided into four stages. The AE signals that occurred during stages I and II are mainly the low-energy signals, and the cumulative released energy curve increases slowly. However, when a small stress drop occurs in stage II, more energy is released, shown as a sudden increase in cumulative release. In stage III, only a slight energy released, and the cumulative released energy curve is almost horizontal. Also, a sudden increase in AE energy was observed at the peak stress point, and the increment is the largest. The energy release characteristic after the peak is similar to the AE activity, intermittent energy release, and smaller contribution to the general cumulative released energy. The AE activity and energy release characteristics of remaining samples are similar to those of the abovementioned slate samples, but the specific values are different. Figs. 11c and 11d show the mean values of maximum AE count rate and

maximum energy release rate of slate with different β values. On the whole, with the increase in β, the AE count rate and energy release rate show a linear decrease, i.e., the energy released by microcracks of slate with vertical bedding is the least, indicating that the generation of tension microcracks along the bedding plane weakens the energy release of microcracks to a certain extent.

Additionally, the relationship of average frequency (AF) and the ratio of rise time to amplitude (RA) are commonly used to distinguish the characteristics (tensile or shear) of microcracks (Zhang and Deng, 2020). In the Cartesian coordinate system of AF-RA, a straight line was observed with a slope of k across the origin, dividing the coordinate system into two parts: The tension and shear microcracks are located above and below the straight line, respectively. However, there is no specific criterion to determine the critical slope (k). If the maximum values of RA and AF are denoted as RA_{max} and AF_{max}, respectively, the slope of diagonal line can be represented by the ratio RA_{max}/AF_{max} (Yue et al., 2020), which depends on the type of material, geometry of specimens, and type of load. In this study, the critical slope is 0.042. Fig. 12a shows the corresponding AF-RA relationship diagram of slate with different β values when the normal stress is 20 MPa. The variation in the ratio of tensile to total microcracks with β is shown in Fig. 12b. As β increases, the ratio first increases, then decreases, and finally increases, and the ratios are all smaller than 50%. When β is 30° and 60°, the ratios are the maximum and minimum, respectively. Additionally, the ratio of slate with vertical bedding is slightly higher than that of horizontal bedding, i.e., the action of shear microcracks of slate sample with $\beta = 0°$ is more obvious than that for sample with $\beta = 90°$.

During direct shear tests, a high degree of stress concentration will occur at both ends of shear fracture. Additionally, the tension induced by shear stress before the nucleation of shear cracks will first produce echelon-shaped cracks (at an angle with shear fracture) at both ends of shear fracture. Therefore, the tensile microcracks account for a certain proportion (less than 50%) for the direct shear tests. For the layered slate, the bedding plane is easier to crack than the matrix, and the cracking of echelon-shaped cracks produced during direct shear is closely related to β. When β is 30° and 60°, tensile cracks along the bedding plane were generated. However, the tensile cracks are more obvious at 30°. Therefore, the proportion of

tensile cracks is relatively high.

When the normal stress is 20 MPa, the AE waveforms corresponding to the peak load of slate with different β values were selected for short-time Fourier transform (Ito and Enoki, 2007) to obtain the two-dimensional frequency spectrum and time-frequency spectrum, as shown in Fig. 13. When β is 0° and 60°, the AE waveform is a long-duration and continuous signal. When β is 30° and 90°, the AE waveform is a short-duration pulse-shaped signal. When β is 0°, the bandwidth of time-frequency spectrum is 220-300 kHz; the duration is about 1 ms; the main frequency is 262 kHz. For β of 90°, the bandwidth is120-190 kHz; the duration is about 0.3 ms; the main frequency is154 kHz. Additionally, the change of main frequency of slate with different β values is shown in Fig. 14. As β increases, the main frequency first decreases, then increases, and finally decreases. A lower frequency indicates the size of microcracks is relatively larger, i.e., the size of microcracks corresponding to vertical bedding is larger than that of horizontal bedding slate.

Moreover, the frequency bandwidth becomes wider and then narrower with the increase in β. When β is 30°, the corresponding bandwidth is the widest, indicating that the span of microcrack size is larger. For horizontally bedding slate, the shear failure along the bedding plane is dominant, and the cohesion of bedding plane is the lowest. The microcracks generated during direct shear include the shearing at the local area and the friction of sheared part. However, for vertical bedding, the shear failure of matrix and bedding plane is the main failure pattern, requiring more energy. Therefore, the frequency of microcracks is lower, i.e., the size of microcracks is relatively larger. Additionally, for oblique bedding, the degree of cracking along the bedding plane results in a difference in microcrack size. From 30° to 60°, the narrowing of bandwidth indicates that the degree of shear failure of matrix is weakened, and the increase in the main frequency indicates that the degree of cracking of bedding plane is enhanced.

4. Conclusion

To explore the deformation and failure mechanism of tunnel layered slate under compression and shear conditions, in this study, the carbonaceous slate of Muzhailing tunnel was selected as the research object, and five sets of direct shear tests were

carried out on the slate with different β values. The strength parameters, shear failure mode, shear fracture topography, energy dissipation, and AE characteristics were analyzed in detail to study the bedding effect of slate failure behavior. The main conclusions are as follows:

(1) As β increases from 0° to 90°, the cohesive angle and internal friction angle of slate increase and decrease linearly, respectively, and the shear strength of bedding plane is lower than that of matrix. Generally, when β is 45°, the corresponding shear strength is the largest. This is mainly because the spacing between bedding planes is large, and the shear body matrix accounts for more. When shear failure occurs, almost no shear-SW phenomenon occurs, and brittle failure is dominant.

(2) The δ of gray-scale image was defined, and the linear corresponding relationship between δ and S_q was established, improving the efficiency of characterizing the fracture topography. Additionally, u_s was estimated, and the dissipated energy is less sensitive to the variation in β. Moreover, u_s is an inherent property of the material itself, and it is less affected by the external load and bedding orientation.

(3) During slate direct shear, the rate of AE counts and energy release rate are closely related to the change in shear stress. When the stress drop occurs, there is a larger count rate, and more energy is released. Additionally, there is a relative quiet period when the peak load is reached. Intermittent AE signals are still observed during the shear sliding in post-peak. The counts rate and energy release rate both linearly decrease with the increase in β. The proportion of tensile microcracks is about 33-45%, and the proportion of tensile microcracks corresponding to vertical bedding is slightly higher than that of horizontal bedding.

(4) The time-frequency characteristics of typical AE waveforms at the peak shear stress show that with the increase in β, the bandwidth of frequency first widens and then narrows. The main frequency values first decrease, then increase, and finally decrease again. The main frequency of vertical bedding is smaller than that of horizontal bedding, i.e., the size of microcracks is relatively larger. Additionally, the frequency bandwidth of slate with β from 30° to 60° becomes narrower, and the increase in main frequency indicates that the degree of shear failure of matrix is weakened. In contrast, the degree of cracking along the bedding plane is enhanced.

Data Availability Statement

All data that support the findings of this study are available from the corresponding author upon reasonable request.

Acknowledgement

Province Education Department of LiaoNing (Grant No. 2020LNQN04) is gratefully acknowledged.

Conflicts of Interest: The authors declare no conflicts of interest.

References

Aliabadian Z, Zhao G and Russel A (2019) Crack development in transversely isotropic sandstone discs subjected to Brazilian tests observed using digital image correlation. International Journal of Rock Mechanics and Mining Sciences 119: 211-221. DOI: 10.1016/j.ijrmms.2019.04.004

Amann F, Button E, Evans K et al. (2011) Experimental study of the brittle behavior of clay shale in rapid unconfined compression. Rock Mechanics and Rock Engineering 44(4):415-430. DOI: 10.1007/s00603-011-0156-3

Babanouri N and Karimi N. (2015) Modeling spatial structure of rock fracture surfaces before and after shear test: a method for estimating morphology of damaged zones. Rock Mechanics and Rock Engineering 48(3):1051-1065. DOI: 10.1007/s00603-014-0622-9

Behrestaghi M, Rao K and Ramamurthy T (1996) Engineering geological and geotechnical responses of schistose rocks from dam project areas in India. Engineering Geology 44(1):183-201. DOI: 10.1016/S0013-7952(96)00069-5

Carey J, Lei Z, Rougier E et al. (2015) Fracture-permeability behavior of shale. Journal of Unconventional Oil and Gas Resources 11:27-43. DOI: 10.1016/j.juogr.2015.04.003

Cheng L, Xu J, Peng S et al. (2019) Mesoscopic crack initiation, propagation, and coalescence mechanisms of coal under shear loading. Rock Mechanics and Rock Engineering 52(6):1979-1992. DOI: 10.1007/s00603-018-1668-x

Claesson J and Bohloli B (2002) Brazilian test: stress field and tensile strength of anisotropic rocks using an analytical solution. International Journal of Rock Mechanics and Mining Sciences 39(8): 991-1004. DOI: 10.1016/S1365-1609(02)00099-0

Cloos M (1992). Thrust-type subduction-zone earthquakes and seamount asperities: a physical model for seismic rupture.

Geology 20(7): 601-604. DOI: 10.1130/0091-7613(1992)0202.3.CO;2

He C (1995) Slip-weakening constitutive relation and the structure in the vicinity of a shear crack tip. Pure and Applied Geophysics 145(3):747-757. DOI: 10.1007/978-3-0348-9065-6_19

Heng S, Yang C, Zeng Y et al. (2014) Anisotropy of shear strength of shale based on direct shear test. Chinese Journal of Rock Mechanics and Engineering 33(5):874-883. (in Chinese)

He M, Nie W, Zhao Z et al. (2012) Experimental investigation of bedding plane orientation on the rockburst behavior of sandstone. Rock Mechanics and Rock Engineering, 45(3), 311-326. DOI: 10.1007/s00603-011-0213-y

Ikari M, Niemeijer A, Marone C (2015) Experimental investigation of incipient shear failure in foliated rock. Journal of Structural Geology 77: 82-91. DOI: 10.1016/j.jsg.2015.05.012

Ito K and Enoki M (2007) Real-time denoising of ae signals by short time Fourier transform and wavelet transform. Journal of Acoustic Emission 25:247-252.

Jaeger J (1960) Shear failure of anisotropic rocks. Geological Magazine 97(1):65-72. DOI: 10.1017/S0016756800061100

James R, Weng X, Yu X et al. (2016) Bedding-plane slip as a microseismic source during hydraulic fracturing. SEG Technical Program Expanded Abstracts 2555-2559.

Ju M, Li J, Li X et al. (2019) Fracture surface morphology of brittle geomaterials influenced by loading rate and grain size. International Journal of Impact Engineering, 103363. DOI: 10.1016/j.ijimpeng.2019.103363

Lisjak A, Garitte B, Grasselli G et al. (2015) The excavation of a circular tunnel in a bedded argillaceous rock (Opalinus Clay): short-term rock mass response and FDEM numerical analysis. Tunnelling and Underground Space Technology incorporating Trenchless Technology Research 45: 227-248. DOI: 10.1016/j.tust.2014.09.014

Liu J, Chen Y, Wan W et al. (2018) The influence of bedding plane orientation on rock breakages in biaxial states. Theoretical and Applied Fracture Mechanics 95:186-193. DOI: 10.1016/j.tafmec.2018.03.005

Maruvanchery V, and Kim E (2020) Effects of a high temperature (500°C) on the fracture processes in calcite-cemented sandstone along bedding-plane orientations. Rock Mechanics and Rock Engineering 53(2): 955-966. DOI: 10.1007/s00603-019-01916-3

Ning Y, An X, Ma G (2011) Footwall slope stability analysis with the numerical manifold method. International Journal of Rock Mechanics and Mining Sciences 48(6):964-975. DOI:10.1016/j.ijrmms.2011.06.011

Ohtsu M (2008) Acoustic Emission Testing. Springer Berlin Heidelberg.

Pomeroy C, Hobbs D, Mahmoud A (1971) The effect of weakness-plane orientation on the fracture of Barnsley Hards by triaxial compression. International Journal of Rock Mechanics and Mining Sciences & Geomechanics Abstracts 8(3): 227-238. DOI: 10.1016/0148-9062(71)90021-0

Ramamurthy T (1993) Strength and modulus responses of anisotropic rocks. Oxford: Pergamon Press 313-325.

Ren F, Zhu C, He M (2020) Moment tensor analysis of acoustic emissions for cracking mechanisms during schist strain burst. Rock Mechanics and Rock Engineering 53(1):153-170. DOI: 10.1007/s00603-019-01897-3

Shen B, Shi J, Barton N (2018) An approximate nonlinear modified Mohr-Coulomb shear strength criterion with critical state for intact rocks. Journal of Rock Mechanics and Geotechnical Engineering 10(4): 37-44. DOI: 10.1016/j.jrmge.2018.04.002

Staněk F, and Eisner L (2017) Seismicity induced by hydraulic fracturing in shales: a bedding plane slip model. Journal of Geophysical Research: Solid Earth 122. DOI: 10.1002/2017JB014213

Sun K, Zhang S, Xin L (2016) Impacts of bedding directions of shale gas reservoirs on hydraulically induced crack propagation. Natural Gas Industry 3(2): 139-145. DOI: 10.1016/j.ngib.2016.03.008

Suo Y, Chen Z, Rahman S et al. (2020) Experimental and numerical investigation of the effect of bedding layer orientation on fracture toughness of shale rocks. Rock Mechanics and Rock Engineering 1-11. DOI: 10.1007/s00603-020-02131-1

Taliercio A, and Landriani G (1988) A failure condition for layered rock. International Journal of Rock Mechanics & Mining sciences and Geomechanics Abstracts 25(5):299-305. DOI: 10.1016/0148-9062(88)90006-X

Tao Z, Cao J, Yang L et al. (2020) Study on deformation mechanism and support measures of soft surrounding rock in Muzhailing deep tunnel. Advances in Civil Engineering 2:1-14. DOI: 10.1155/2020/9367916

Tatone B, and Grasselli G (2015) Characterization of the effect of normal load on the discontinuity morphology in direct shear specimens using X-ray micro-CT. Acta Geotechnica 10(1):31-54. DOI: 10.1007/s11440-014-0320-5

Tien Y，Kuo M. (2001) A failure criterion for transversely isotropic rocks. International Journal of Rock Mechanics and

Mining Sciences 38(3):399-412. DOI: 10.1016/S1365-1609(01)00007-7

Virgo S, Abe S, Urai J (2013) Extension fracture propagation in rocks with veins: insight into the crack-seal process using discrete element method modeling: DEM fracture-vein interaction. Journal of Geophysical Research Solid Earth 118(10): 5236-5251. DOI: 10.1002/2013JB010540

Xie J, Tang J, Yong R et al. (2020) A 3-D hydraulic fracture propagation model applied for shale gas reservoirs with multiple bedding planes. Engineering Fracture Mechanics 228:106872. DOI: 10.1016/j.engfracmech.2020.106872

Yue J, Kunnath S, Xiao Y (2020) Uniaxial concrete tension damage evolution using acoustic emission monitoring. Construction and Building Materials 232:117281. DOI: 10.1016/j.conbuildmat.2019.117281

Zhang Z, Deng J (2020) A new method for determining the crack classification criterion in acoustic emission parameter analysis. International Journal of Rock Mechanics and Mining sciences 130:104323. DOI: 10.1016/j.ijrmms.2020.104323

Zhao Y, Zhang L, Wang W et al. (2017) Transient pulse test and morphological analysis of single rock fractures. International Journal of Rock Mechanics and Mining Sciences, 91:139-154. DOI: 10.1016/j.ijrmms.2016.11.016

Zhu C, He M, Karakus M et al. (2020) Investigating toppling failure mechanism of anti-dip layered slope due to excavation by physical modelling. Rock Mechanics and Rock Engineering, DOI:10.1007/s00603-020-02207-y

Figures

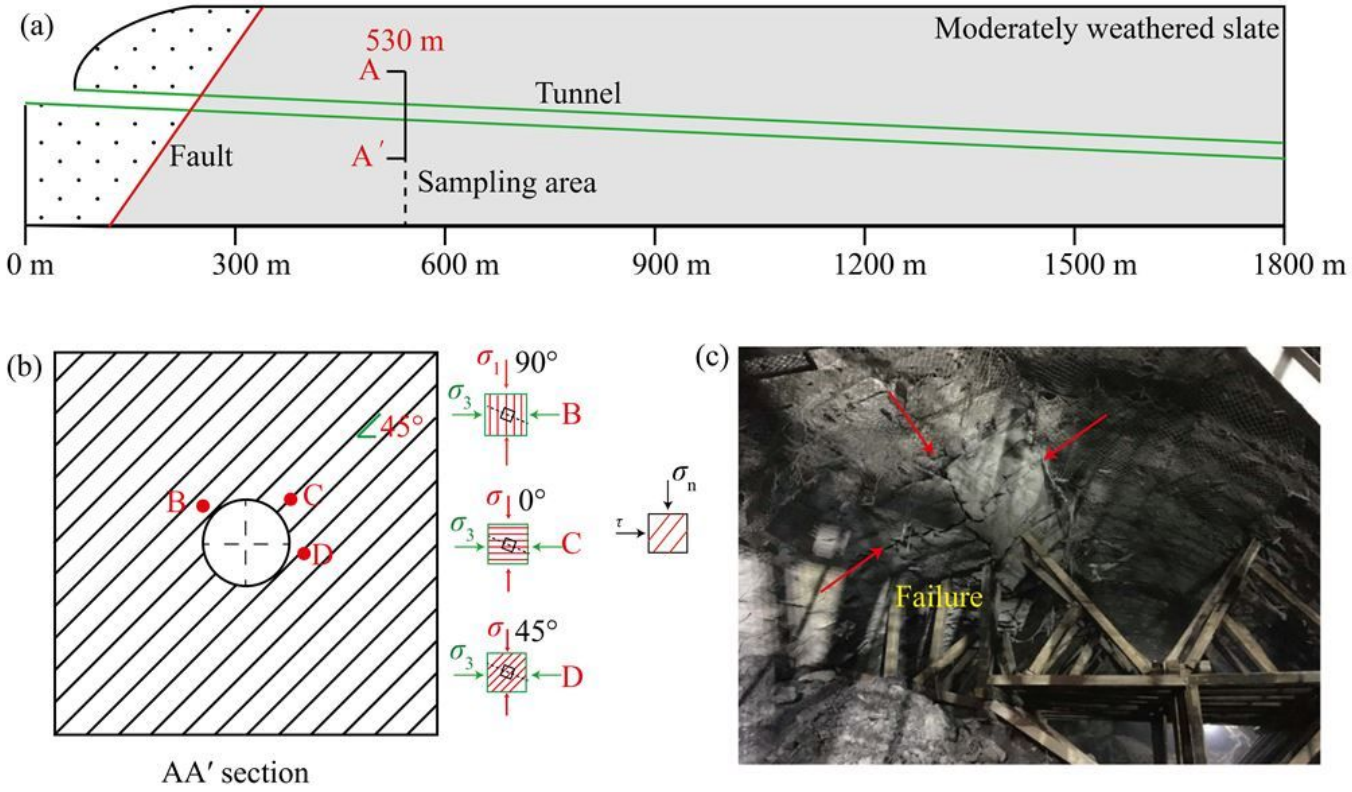

Figure 1

(a) Engineering geology profile of Muzhailing tunnel, (b) diagram of bedding plane angle (β) of rock element at different locations of tunnel section, and (c) severe deformation in the left shoulder of tunnel

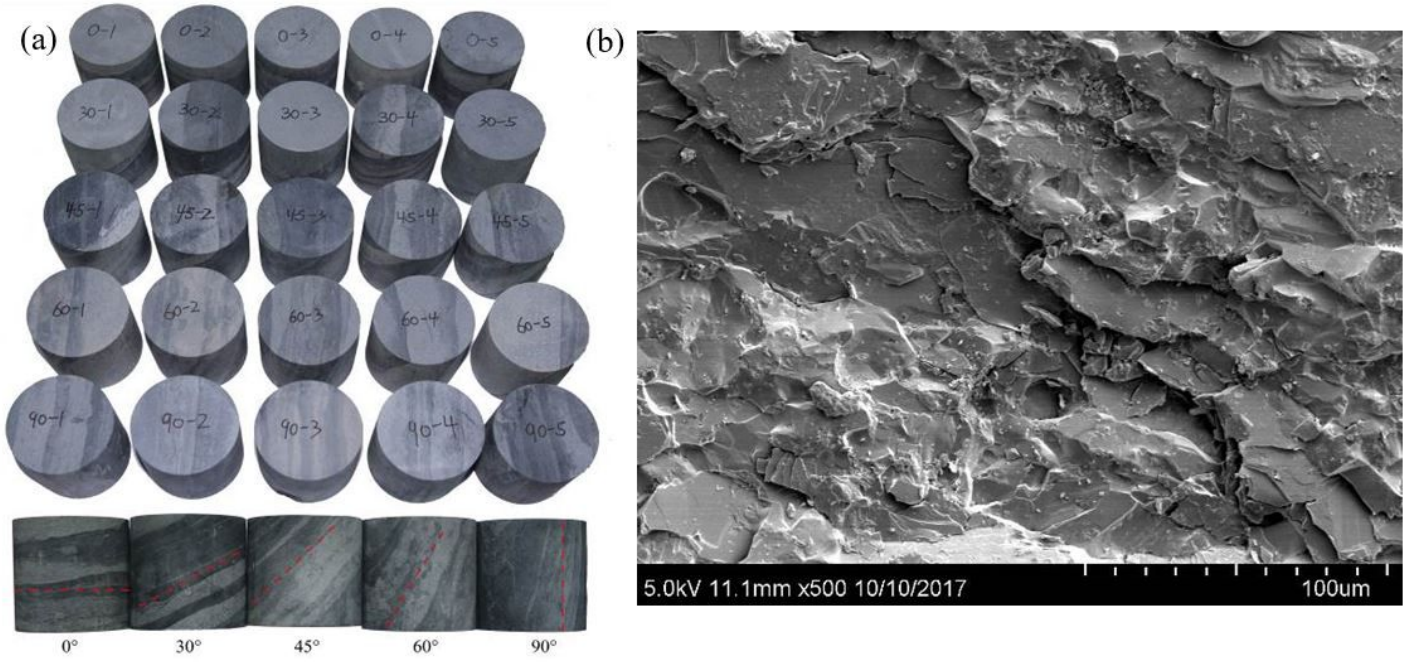

Figure 2

(a) Slate samples for direct shear test, and (b) microscopic structure of the slate

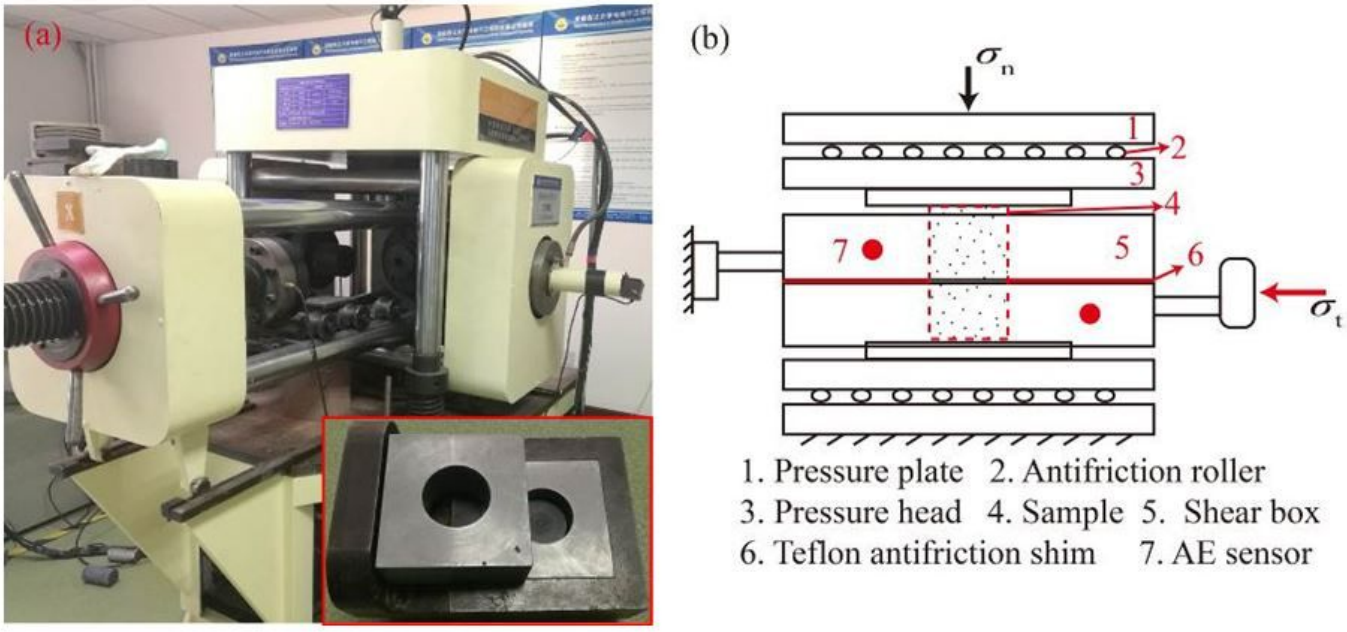

Figure 3

(a) Ture triaxial loading system and shear box, and (b) schematic of principal of the shear box

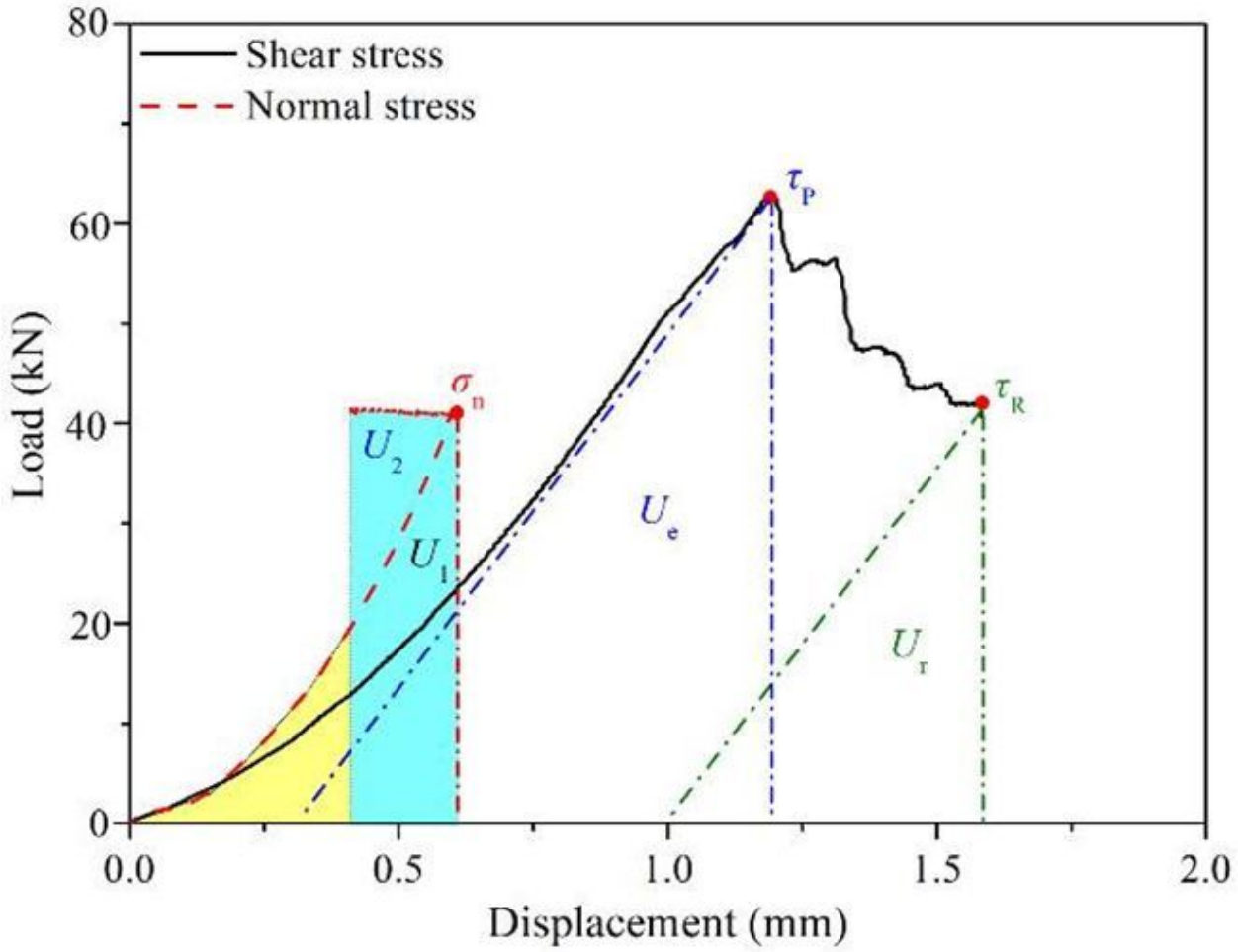

Figure 4

Schematic of strain energy calculation for the direct shear test

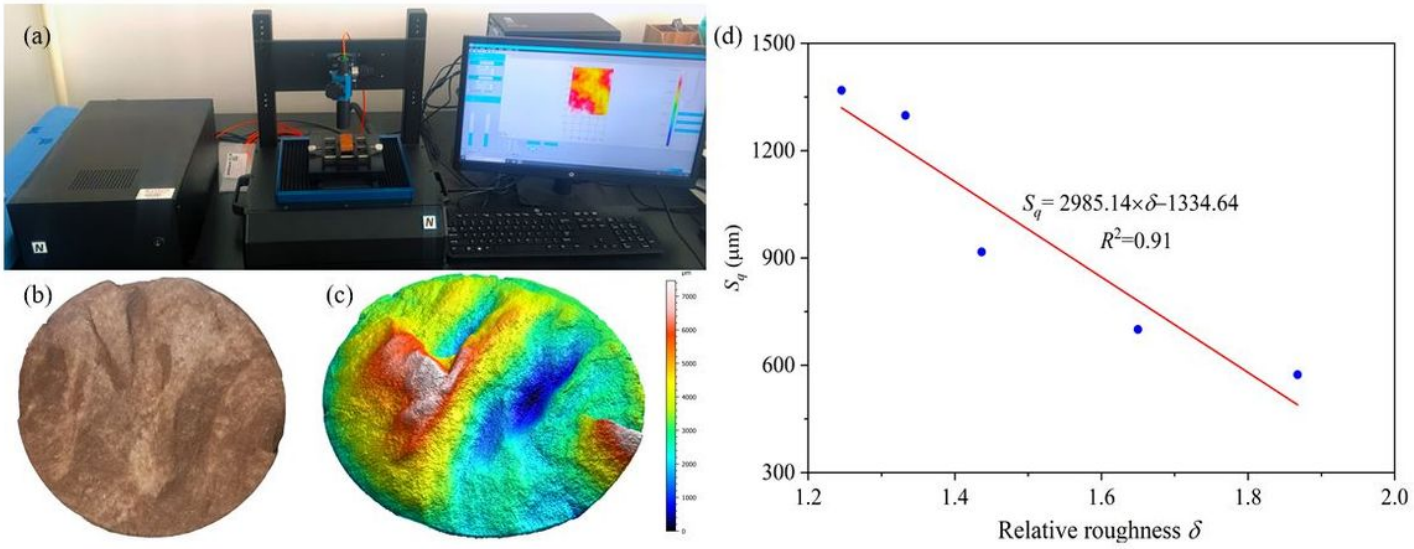

Figure 5

(a) Three-dimensional noncontact surface profiler, (b) photograph and (c) three-dimensional topography of shear fracture, and (d) relationship between Sq and δ

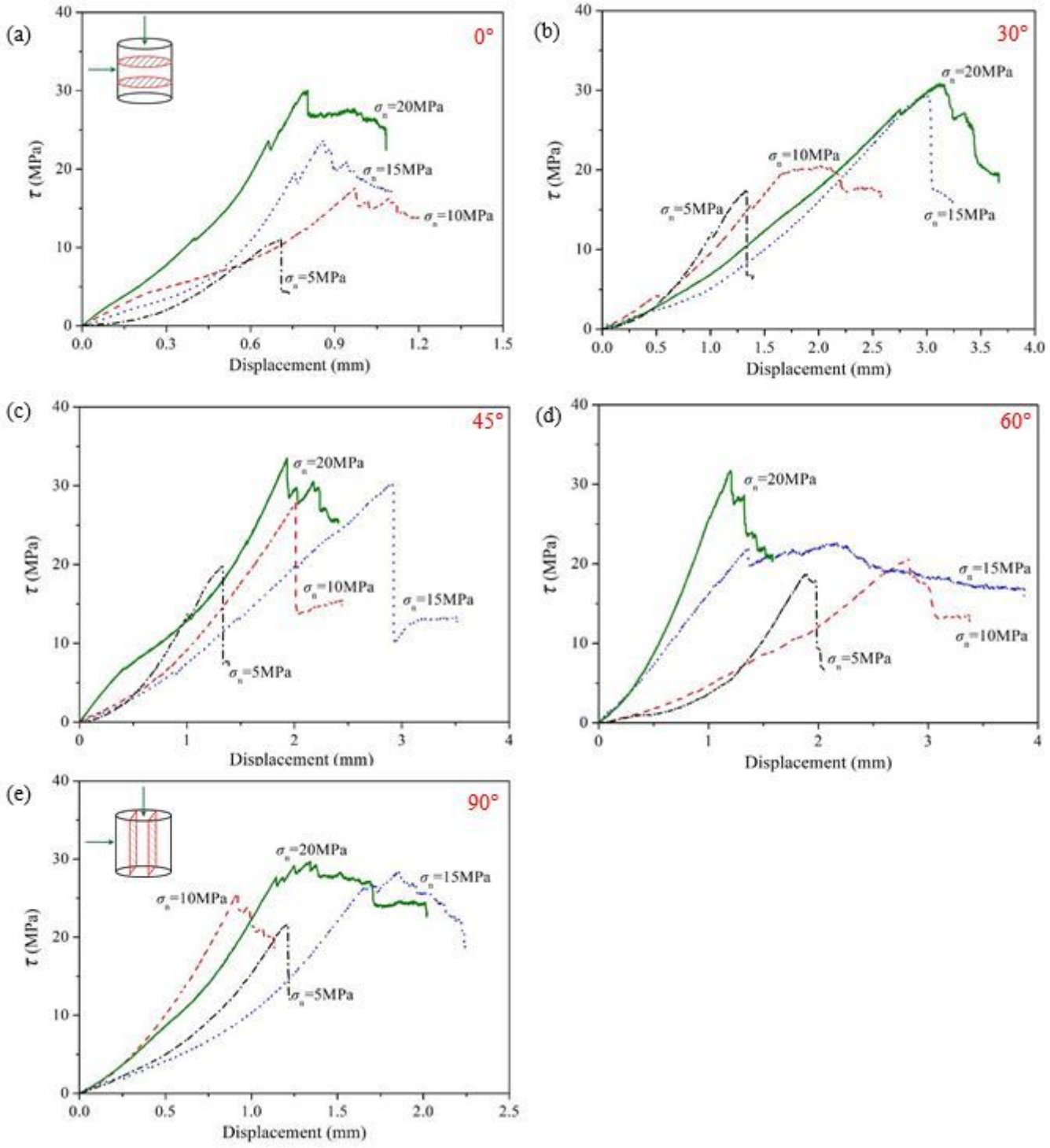

Figure 6

The curves of shear stress-displacement for slate with β under four normal stresses; (a~e) 0°, 30°, 45°, 60° and 90°, respectively.

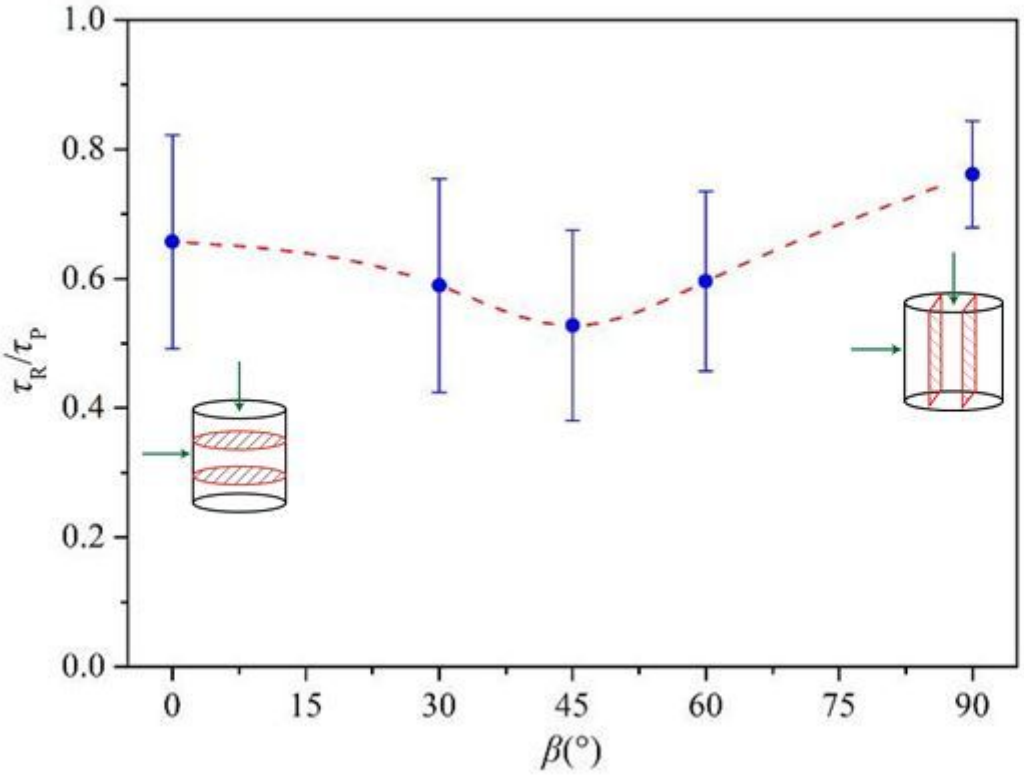

Figure 7

Variation of ratios of residual to peak shear strength with β

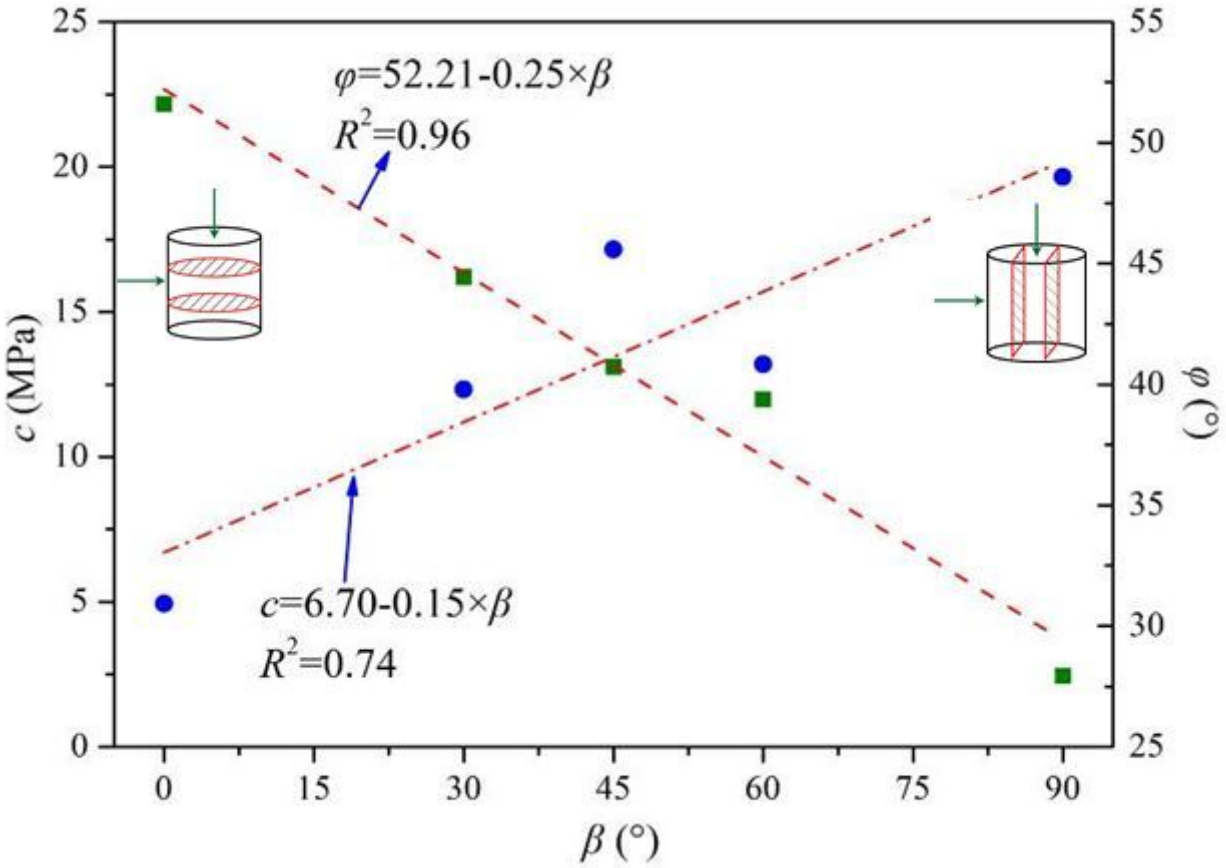

Figure 8

Relationship between shear strength parameters and β

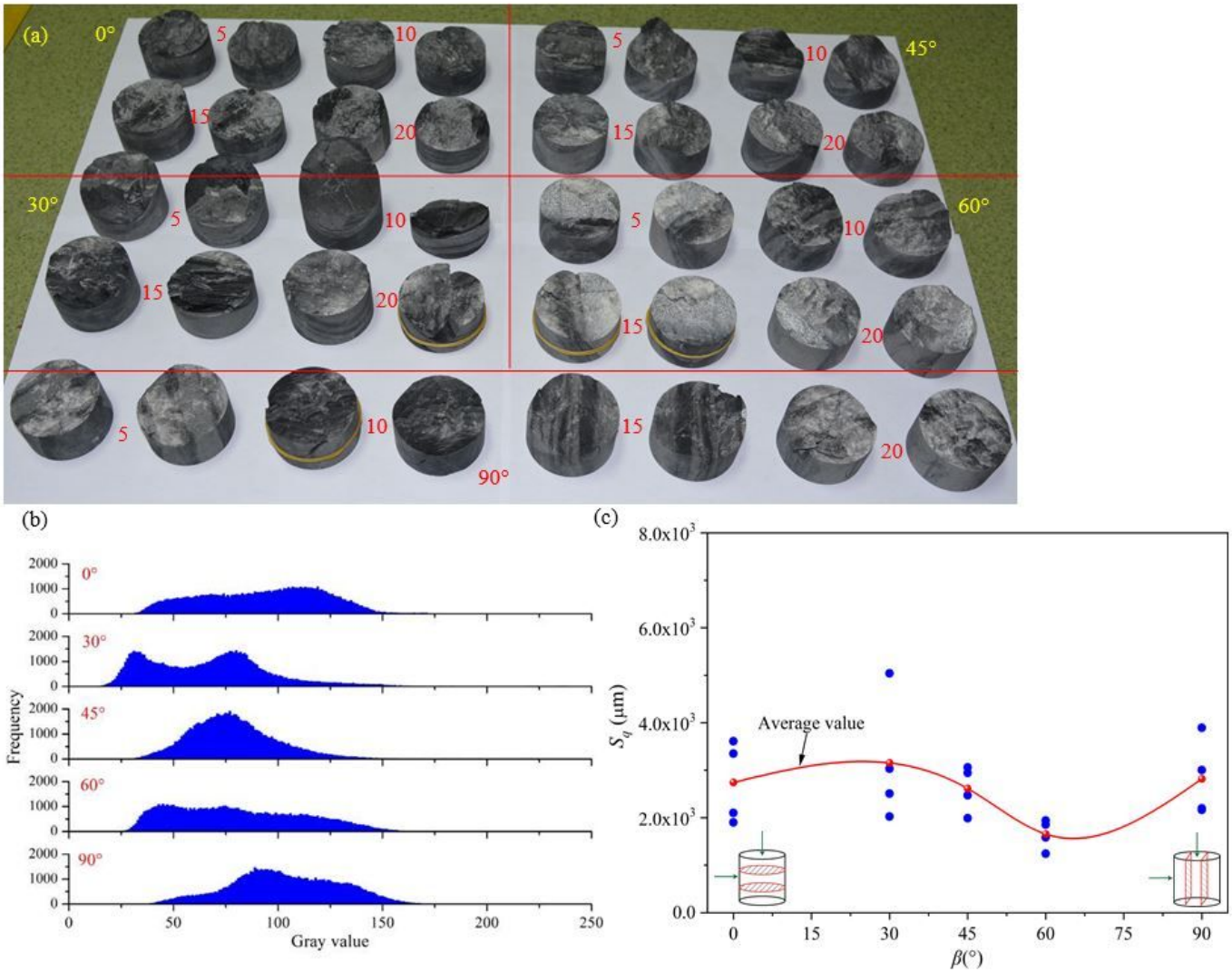

Figure 9

(a) Failure photographs of slate after direct shear tests, (b) gray histogram of typical failure fracture, and (c) the relationship between Sq and β

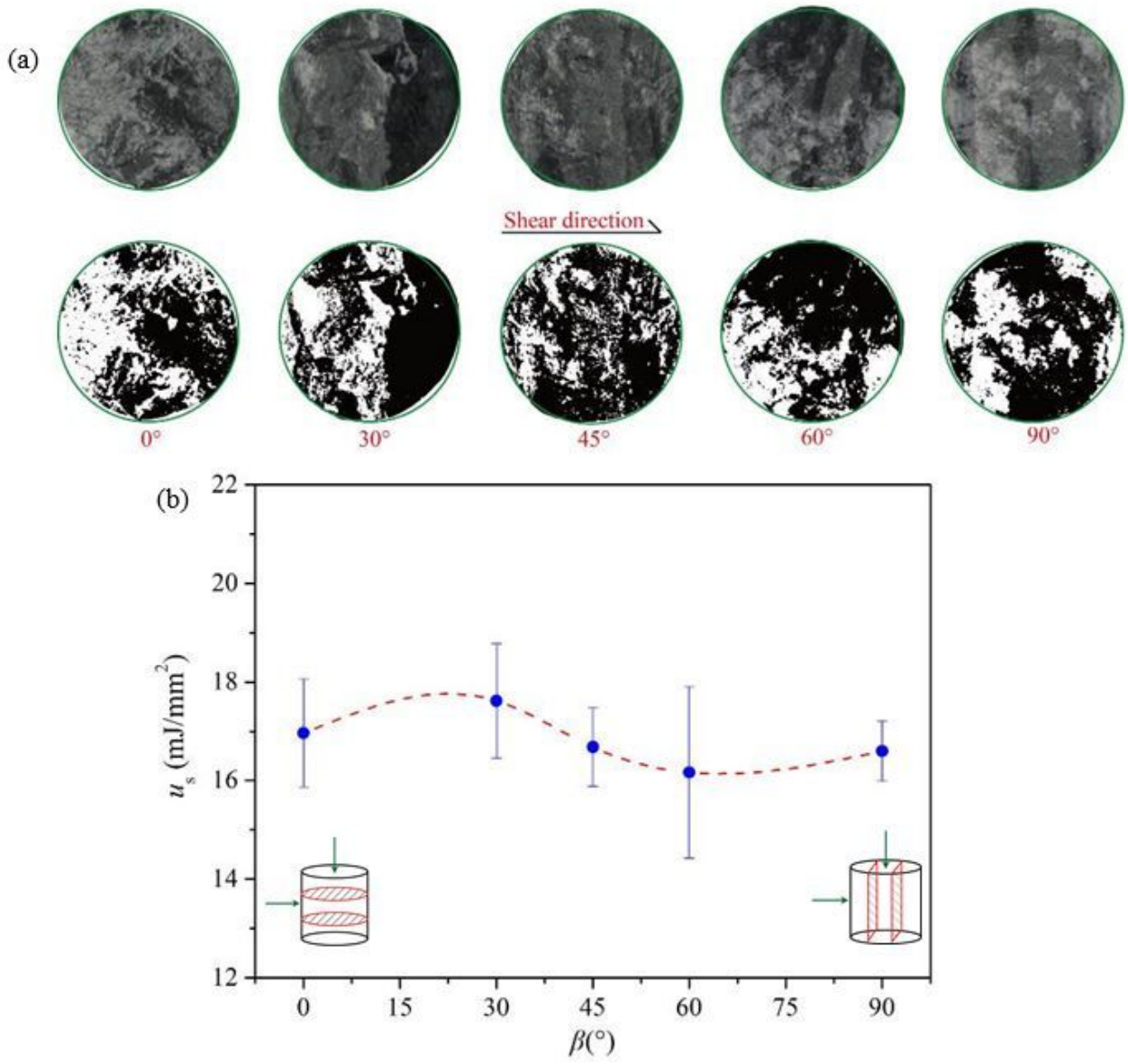

Figure 10

(a) Photographs and grayscale images of shear fractures, and (b) the relationship between us and β

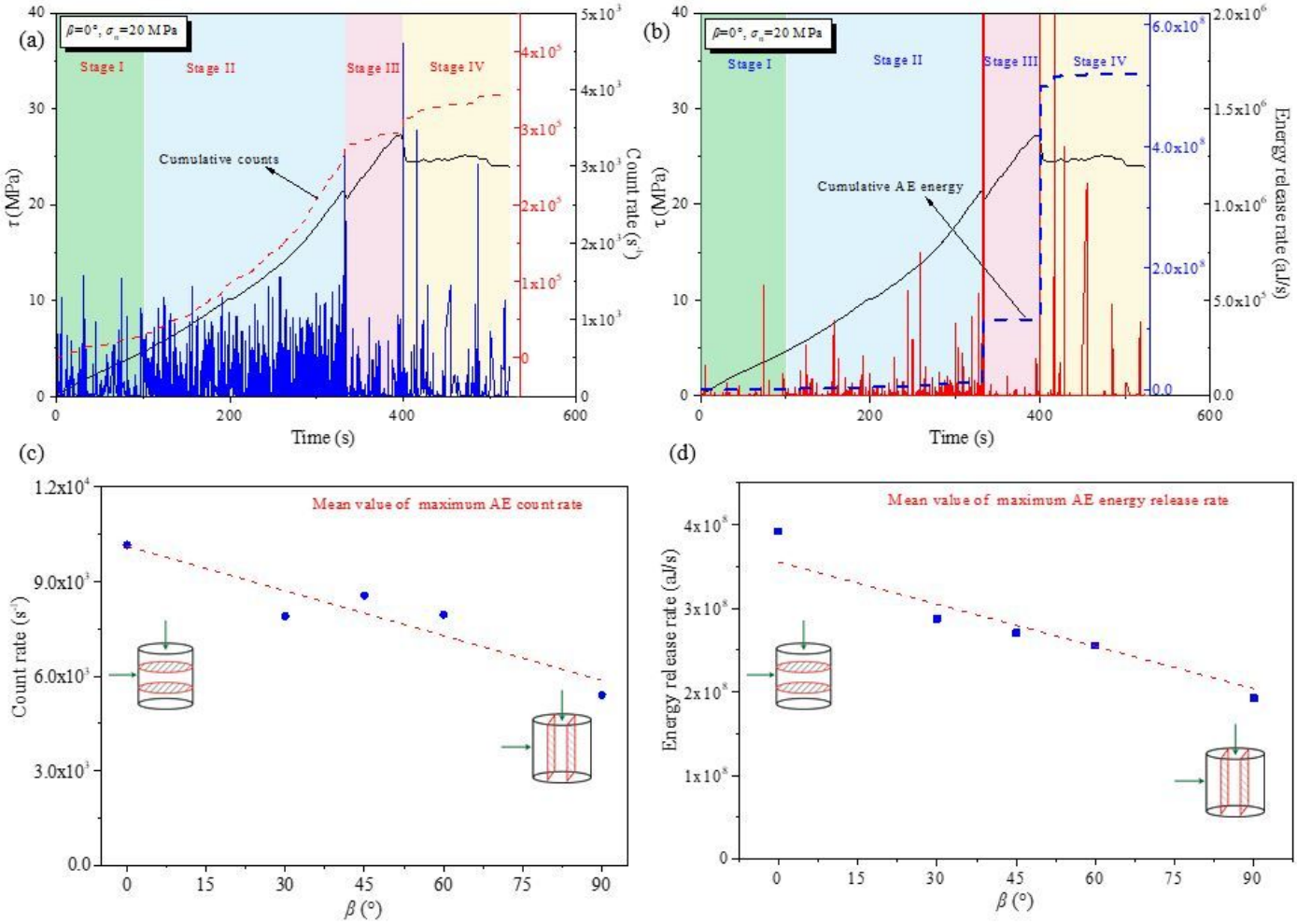

Figure 11

Evaluation of (a) AE count rate and (b) energy release rate of slate (β = 0°, σn = 20 MPa) with time elapse; relationship between mean value of maximum (c) AE count rate, and (d) AE energy release rate and β

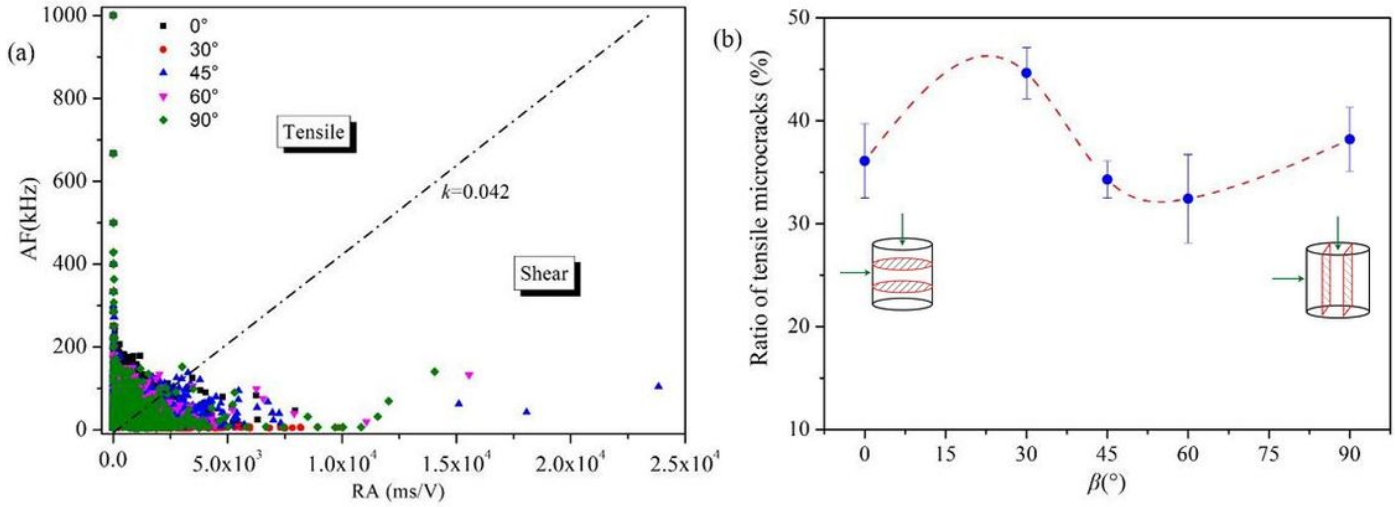

Figure 12

(a) Scatter diagram of AF and RA, and (d) variation of the ratios of tensile microcracks with β

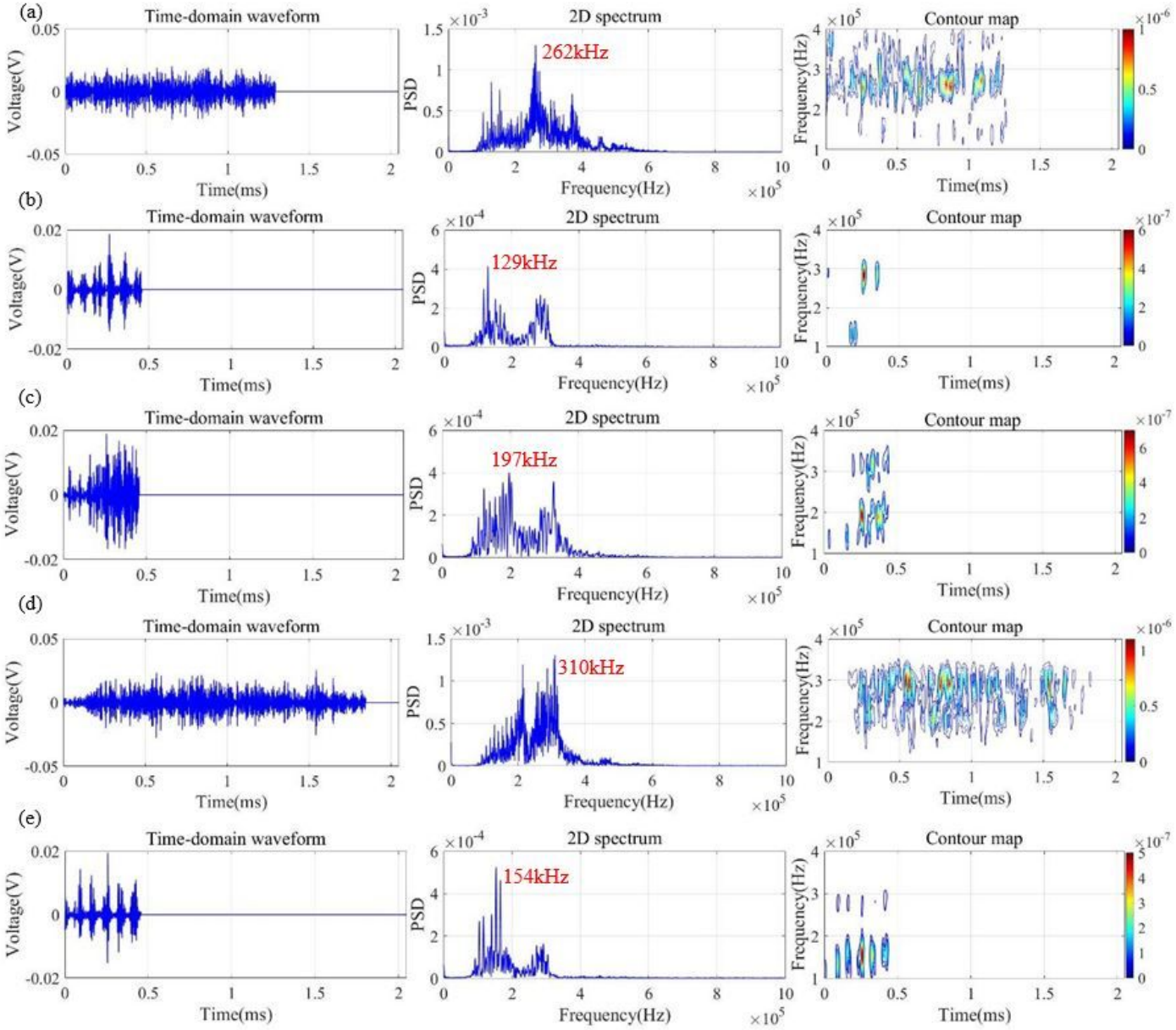

Figure 13

Typical waveform, spectrum and corresponding time-spectrum of AE signals appearing at peak loads (a~e) respectively for 0°, 30°, 45°, 60° and 90°

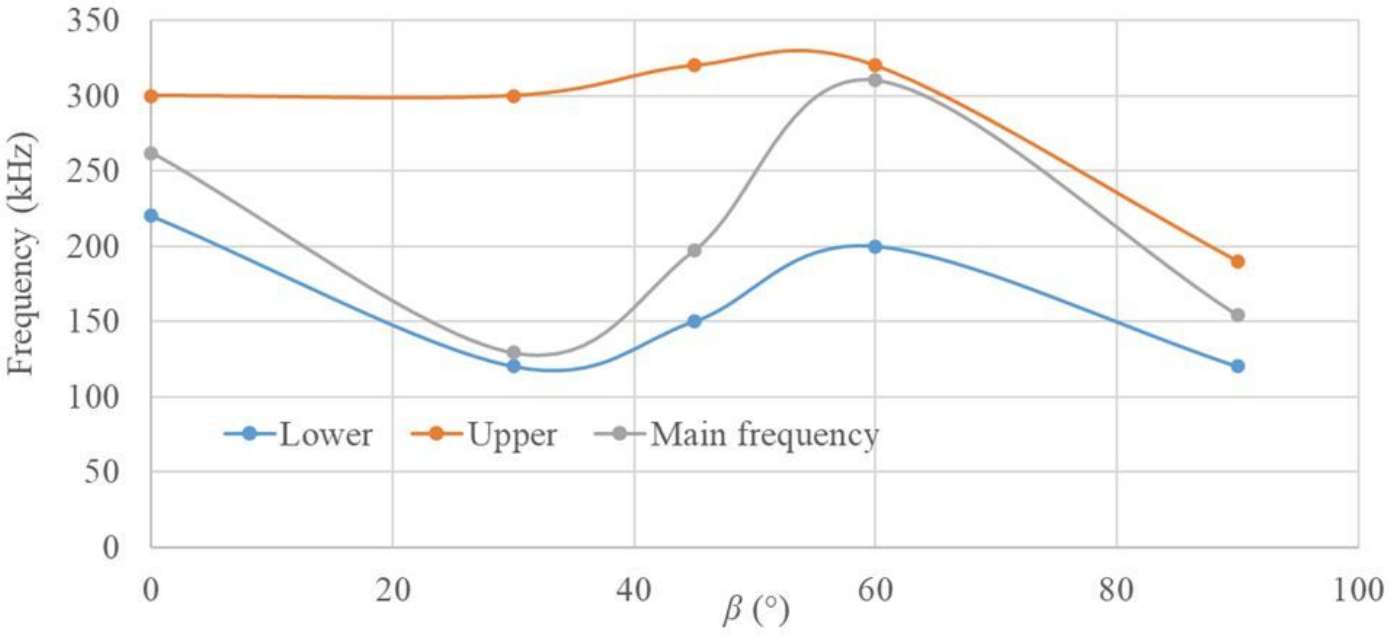

Figure 14

Variation of frequency band of typical AE waveforms with β